Supplementary Information

Periodic bicontinuous composites for high specific energy absorption

Jae-Hwang Lee[1,3,4], Lifeng Wang[2,3,5], Mary C. Boyce[2,3], and Edwin L. Thomas[1,3,4,]*

[1]Department of Materials Science and Engineering, MIT, Cambridge, Massachusetts 02139, USA

[2]Department of Mechanical Engineering, MIT, Cambridge, Massachusetts 02139, USA

[3]Institute for Solider Nanotechnologies, MIT, Cambridge, Massachusetts 02139, USA

[4]Department of Mechanical Engineering and Materials Science, Rice University, Houston, Texas 77005, USA

[5]Department of Civil and Environmental Engineering, Clarkson University, Potsdam, New York 13699, USA

***** E-mail: elt@rice.edu

1. Fabrication scheme of PnF, CnF, and CPnF

The PnF is fabricated using a negative SU8 photoresist employing interference lithography and additional crosslinking as described in our previous report.[1] To create the CnF, the PnF on a uniform SU8 film is then placed between two perforated aluminum plates with a gap of 100 μm to allow lateral shrinkage without bending of the film and heated to 300 °C at a ramping rate of 5 °C/min in air and held for an hour to stabilize the sample, then cooled down. Next, without the aluminum plates, the stabilized sample is heated to 1000 °C at a ramping rate of 5 °C/min in high vacuum (~10^{-6} Torr) and held for an hour before cooling. The porosity of the CnF can be estimated with SEM images after vertically cross sectioning by FIB milling while the porosity of the PnF is determined by using infrared reflection spectrum.[1] There is not much change in the porosity after carbonization due to the anisotropic shrinkage. To create the CPnF, epoxy is infiltrated into the submicron-pores of a CnF on a carbon film using a low viscosity, two-part thermally-crosslinkable epoxy-B (No.635/No.556, US Composites Inc.). To further reduce the viscosity, toluene is added to the resin and hardener with a weight ratio of hardener:resin:toluene of 1:2:3. A CnF sample is placed in a low vacuum chamber and then the diluted epoxy-B is applied to the top of the sample to backfill and to reduce the possibility of air entrapment. After removing the toluene in the sample by leaving the sample in the vacuum chamber for 30 min, the excess uncured epoxy-B on the top of the sample is removed by a rubber blade but leaves a thin (less than 1 μm) layer of epoxy-B. The epoxy-B-filled carbon sample (CPnF) is then cured at 75 °C for 24 hrs in an oven.

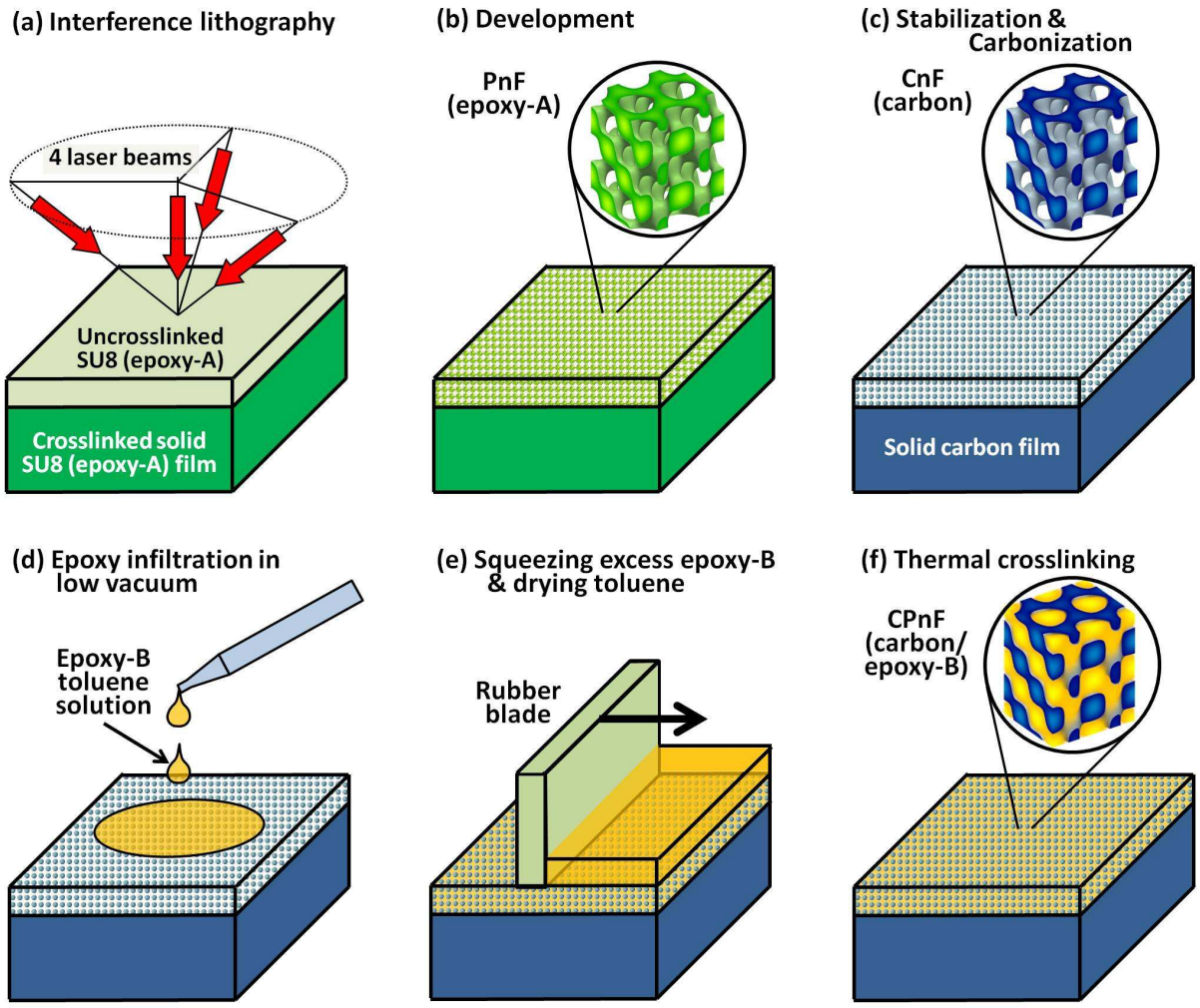

Figure S1. Schematic of fabrication. (a) SU8 photoresist on a crosslinked SU8 film is exposed to the 4 beams of laser and selectively crosslinked following the intensity distribution of 3D interferogram. (b) Crosslinked SU8 remains after development and becomes PnF. (c) The PnF on a SU8 film is oxidized for 1 hr at 300 °C in air and carbonized at 1000 °C for 1hr to result CnF on a solid carbon film. (d) Epoxy-B solution is applied on the surface of CnF under low vacuum to avoid air trapping. (e) Excessive epoxy-B on the surface is removed by a rubber blade made of PDMS (Sylgard 184, Dow Corning). (f) CPnF is achieved after crosslinking infiltrated epoxy-B thermally.

2. Mechanical properties of SU8 and carbonized SU8

SU8 (epoxy-A) films (0.5mmx10mmx6μm) and carbonized SU8 films (0.35mmx10mmx4.5μm) were tensile-tested to have Young's modulus depending on carbonization temperatures. Stress-strain curves changed significantly in Fig. S2a as the carbonization temperature increased. Compared to largely plastic deformation of cross-linked SU8 films over 15% of strain, carbonized SU8 became stiffer and more brittle as increasing the temperature. The Young's modulus of SU8 varied from 2.7GPa to 30GPa at 1000°C in Fig. S2b, where the modulus was calculated from the initial slop of each curve in the stress-strain plot. The surface of a 1000°C-carbonized SU8 film was patterned to have micro-pillars (~1μm diameter, 1.5μm height) by FIB milling as seen in the inset of Fig. S2c. Three carbon pillars were compressed to three different displacements, 100, 200, and 400nm and load-displacement curves were converted to stress-strain curves after correction of substrate deformation in Fig. S2d. The elastic moduli of 26 GPa and 32 GPa from the loading and unloading curves respectively, which showed a good agreement with the Young's modulus from the macroscopic tensile tests in Fig. S2b. The carbon pillars showed both a large yield stress of 3.3 GPa at a high strain of 14%.

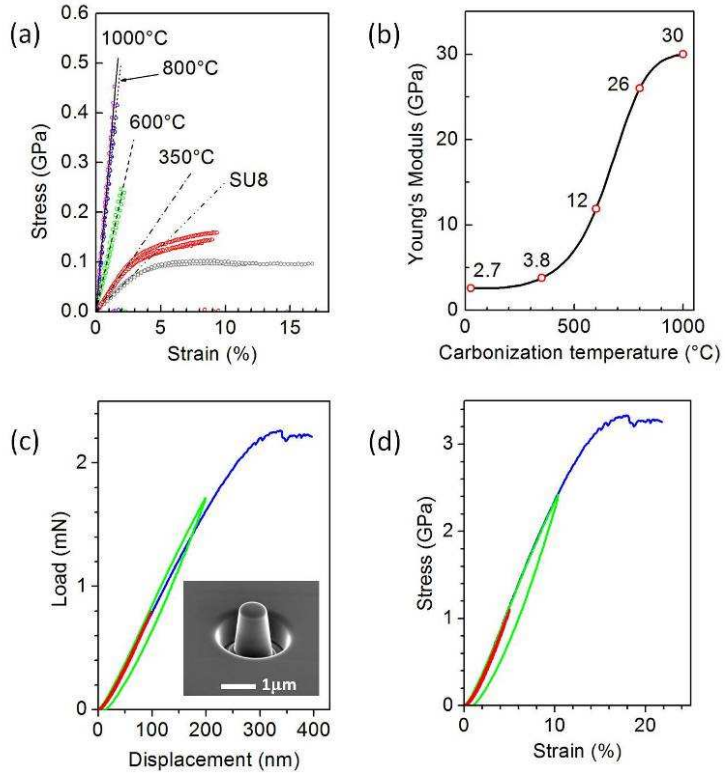

Figure S2. Mechanical properties of carbonized SU8. (a) Stress-strain curves for different carbonization temperatures (b) Young's moduli for four different carbonization temperatures. (c) Load-displacement curves from three carbon pillars, compressed to three different displacements. (d) Stress-strain curves of the three carbon pillars.

3. Microscopic uniaxial compression tests.

A dual-beam FIB milling machine (Helios NanoLab 600, FEI) was used for making the pillars and recording the high resolution SEM images. Generally FIB milling was carried out in two steps; a fast milling (30kV, 2.8nA) for the surrounding area and a slow milling (30kV, 9.7pA) for final cuts to reduce ion beam damage to the pillars. Since a CPnF sample had about 1μm thick epoxy-B layer on top, an extra step for removing the top layer was performed prior to the two

steps of milling. SEM images are taken at 52° tilt at 5kV in the immersion mode. Samples containing PnF pillars on SU8 film and CnF and CPnF pillars on carbon film were mounted on a 1.5mm thick glass plate with glue for the compression tests. We used a 11μm diameter diamond flat indenter (TI950 TriboIndenter, Hysitron Inc.) to apply a load to the pillars with the maximum loads, 0.6mN and 1.2mN. Although the kinetic energy carried by scattered fragments of the PnF and CnF should be excluded in the rigorous estimation of energy absorption as this energy is not dissipated in the compression event, we ignore the contribution. Ideally the area enclosed in the load-displacement plot by one cycle of loading and unloading represents the energy absorption by a pillar; however, this estimate has a limitation because there are no data points during pillar collapse since the collapse time is much shorter than the data acquisition interval of 15 ms. Thus, area bounded by the loading/unloading curves should be considered as the upper limit of energy absorption.

4. Mechanical properties of epoxy-B pillars

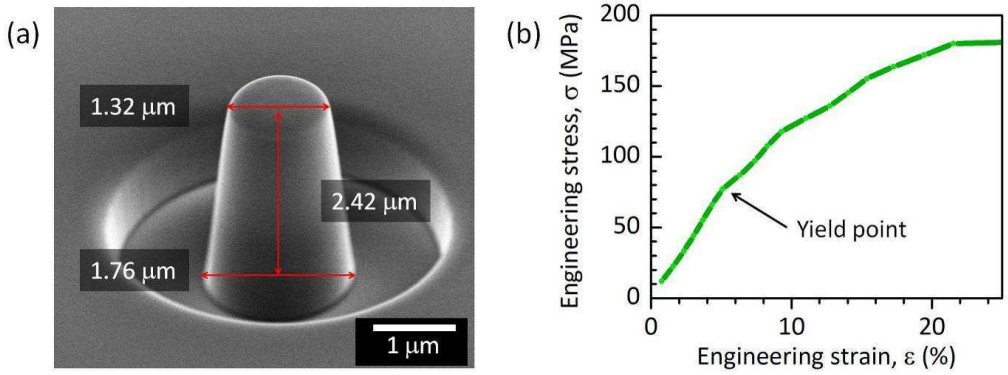

Figure S3. Mechanical properties of epoxy-B. (a) The SEM image shows an epoxy-B pillar of 2.42 μm height and 1.54 μm average diameter. (b) Stress-strain curve of the epoxy-B pillar shows Young's modulus of 1.4 GPa and a yield stress of 80 MPa.

5. Finite-element based micromechanical modeling

In order to understand the underlying mechanisms that govern the deformation of nanoframe structures, micromechanical models are constructed and deformed based on periodic Representative Volume Elements (RVEs) using finite element analysis (FEA). The RVE is chosen as the repeating cell of the nanoframe structure together with periodic boundary conditions to fully simulate the deformation of the microstructure, as shown in **Figure S4**. FEA of micromechanical models of a RVE uses the fabricated geometry of a 65% solid volume fraction and the measured material properties of solid carbon (Young's modulus of 26 GPa, a yield stress of 3.3 GPa) and 35 % solid epoxy-B (Young's modulus of 1.4 GPa and a yield stress of 80 MPa) (see SI). The RVE is space-filling and spatially periodic. When an RVE is subjected to a macroscopic deformation loading, periodic boundary conditions must be applied to the surface of the RVE to ensure compatibility. For example, when the RVE is subjected to a macroscopic deformation gradient, **F**, considering a periodically repeating point pair *A* and *B* located on the surface of the RVE, as shown in **Figure S5**, the relative displacement is determined by the macroscopically applied macroscopic displacement gradient, **H** = **F** – **1**, through

$$\mathbf{u}(B)-\mathbf{u}(A)=(\mathbf{F}-\mathbf{1})\{\mathbf{X}(B)-\mathbf{X}(A)\}=\mathbf{H}\{\mathbf{X}(B)-\mathbf{X}(A)\}, \qquad (1)$$

where **u** denotes the periodic part of the displacement on the boundary surfaces and it is dependent on the applied global loads, **X** denotes position in the reference configuration. Point pairs on opposing periodic surfaces are related to one another using Equation (1). These constraint equations are implemented within the finite element analysis using linear nodal displacement constraint equations in the finite element code ABAQUS. The macroscopic deformation of the RVE is imposed by prescribing the nine components of **F**. Virtual work is

used to calculate the average macroscopic response of the overall RVE. The microscopic first Piola-Kirchhoff stress tensor, **S**, and the corresponding macroscopic Cauchy stress tensor, **T**, can be calculated through the reaction forces of the fictitious nodes which are assigned displacement components according to the displacement gradient. The RVE can be subjected to any arbitrary macroscopic deformation gradient in the finite element analysis. In order to apply these periodic boundary conditions to the RVE surfaces, the mesh on the opposite boundary surfaces must be compatible. In our study, we focus on the macroscopic deformations of uniaxial tension. In the case of uniaxial tension, the macroscopic deformation gradient is given by

$$\mathbf{F} = \lambda_1(t)\mathbf{e}_1 \otimes \mathbf{e}_1 + \lambda_2(t)\mathbf{e}_2 \otimes \mathbf{e}_2 + \lambda_3(t)\mathbf{e}_3 \otimes \mathbf{e}_3 . \tag{2}$$

where λ_1 and λ_2 are un-prescribed, and λ_3 is prescribed to impose a constant macroscopic axial strain rate.

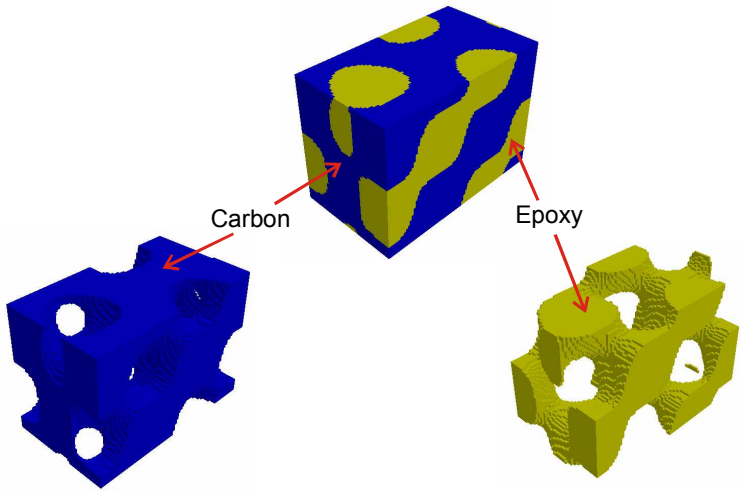

Figure S4. RVE used in the FEA simulation for CPnF and CnF.

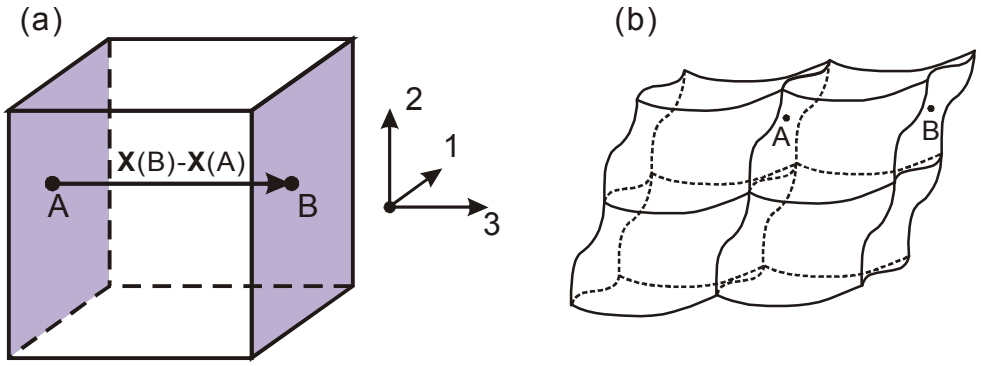

Figure S5. A spatially periodic RVE: (a) Undeformed RVE; (b) deformed RVE with its periodic neighbors

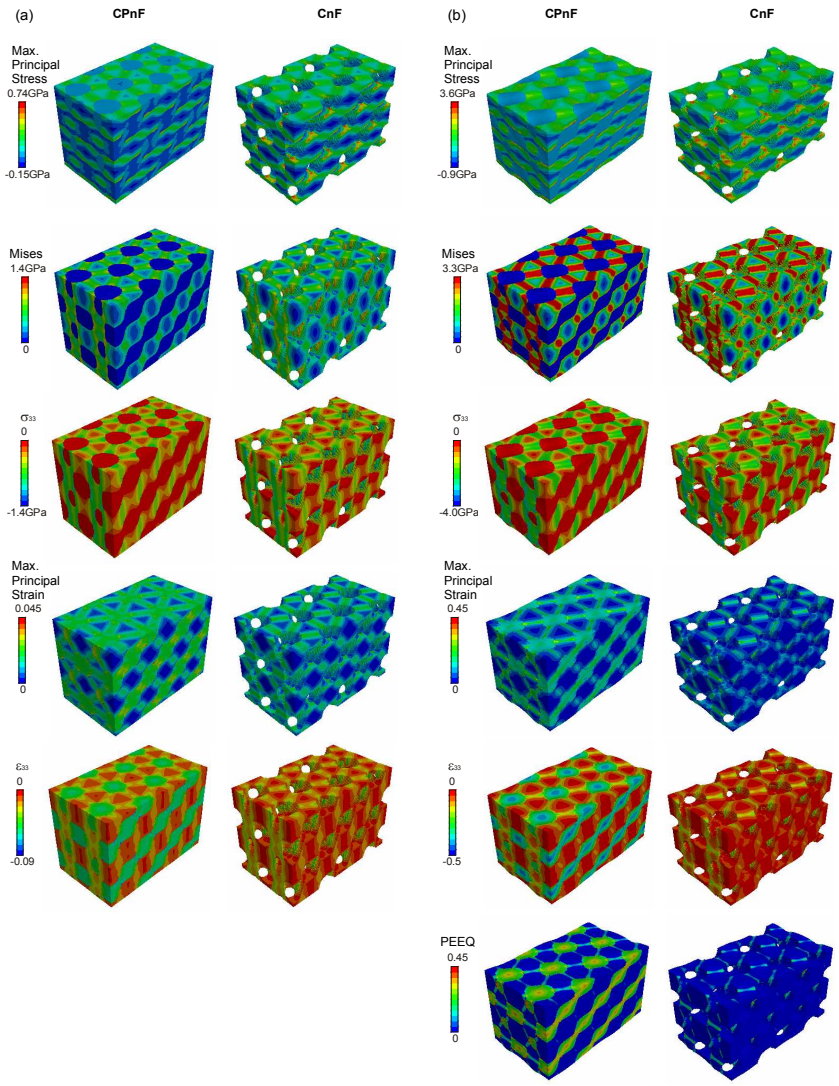

Figure S6. FEA simulation results of CPnF and CnF under uniaxial compression. (a) Contours of maximum principal stress, von Mises stress, axial stress, maximum principal strain, and axial strain of CnF and CPnF (8 RVEs) at a strain of 3%, which is in the elastic region. (b) Contours of maximum principal stress, von Mises stress, axial stress, maximum principal strain, axial strain and equivalent plastic strain of CnF and CPnF (8 RVEs) at a strain of 15%, which is in the plastic region.

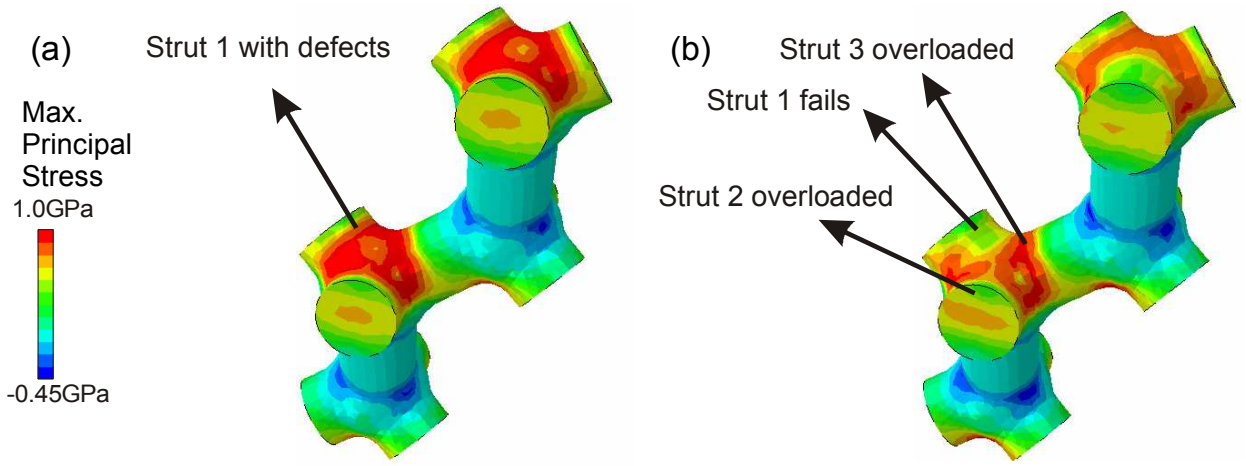

Figure S7. FEA simulation results of CnF (30% volume fraction with same symmetry) under uniaxial compression considering carbon as a brittle material where imperfection is introduced in one strut member (slightly thinner): (a) and (b) show maximum principal stress at the points prior to failure (7% strain) and after failure (8% strain), respectively. Under compression, all struts 1-3 experience same loading and deformation history prior to the failure due to the geometrical symmetry. After the failure criterion is reached, the contours indicate that the strut with imperfection (strut 1) fails and starts to fracture first due to reaching the maximum principal stress. Then the neighboring struts (struts 2 and 3) would overload and fracture, and the whole structure crumbles later (as happens in the experiments).

References

(1) Lee, J. H.; Wang, L. F.; Kooi, S.; Boyce, M. C.; Thomas, E. L. *Nano Lett.* **2010**, 10, 2592.